Supplemental Material for "Collision-induced broadband optical nonreciprocity"

Chao Liang,[1] Bei Liu,[1] An-Ning Xu,[1] Xin Wen,[1] Cuicui Lu,[2,3]
Keyu Xia,[4] Meng Khoon Tey,[1,5] Yong-Chun Liu,[1,5,*] and Li You[1,5]

[1]*State Key Laboratory of Low Dimensional Quantum Physics, Department of Physics, Tsinghua University, Beijing 100084, China*
[2]*Key Laboratory of Advanced Optoelectronic Quantum Architecture and Measurements of Ministry of Education, Beijing Key Laboratory of Nanophotonics and Ultrafine Optoelectronic Systems, School of Physics, Beijing Institute of Technology, Beijing 100081, China*
[3]*Collaborative Innovation Center of Light Manipulations and Applications, Shandong Normal University, Jinan 250358, China*
[4]*College of Engineering and Applied Sciences, Nanjing University, Nanjing 210093, China*
[5]*Frontier Science Center for Quantum Information, Beijing 100084, China*

This Supplemental Material provides (i) theoretical model of the demonstrated optical nonreciprocity (Sec. I), (ii) details about our experimental implementation (Sec. II), and (iii) some additional experiment results (Sec. III).

Contents

I. THEORETICAL MODEL

In this section, we describe the theoretical model for studying nonreciprocal transmission. As discussed in the main manuscript, the system involves three lasers coupled to an ensemble of thermal atoms. The atoms have two ground states $|1\rangle$ and $|3\rangle$ and two excited states $|2\rangle$ and $|4\rangle$. The transition of $|1\rangle \Leftrightarrow |2\rangle$ and $|3\rangle \Leftrightarrow |2\rangle$ are driven by the strong switching and coupling laser beams with the wave number k_s, k_c and the Rabi frequency Ω_s, Ω_c, respectively. The probe laser drives the transition $|3\rangle \Leftrightarrow |4\rangle$, with a wave number k_p and a Rabi frequency Ω_p. The probe laser is weak compared with the switching and coupling lasers, i.e., $\Omega_p \ll (\Omega_c, \Omega_s)$. The corresponding laser detunings are $\Delta_s, \Delta_c, \Delta_p$ for stationary atoms. Under the rotating-wave approximation, the Hamiltonian of the four-level atom interacting with the coupling laser, switching laser, and probe laser in a rotating frame is written as (let $\hbar = 1$)

$$H = -\Delta_s\sigma_{11} - \Delta_c\sigma_{33} + (\Delta_p - \Delta_c)\,\sigma_{44} + \frac{1}{2}\left(\Omega_s\sigma_{21} + \Omega_c\sigma_{23} + \Omega_p\sigma_{43} + H.c.\right), \tag{1}$$

where $\sigma_{nm} = |n\rangle\langle m|\,(n, m = 1, 2, 3, 4)$ are the atomic transition operators. The dynamics of the system can be obtained by solving the master equation given by

$$\dot{\rho} = -i\,[H, \rho] + \mathcal{L}[\rho], \tag{2}$$

where $\mathcal{L}[\rho]$ is the Lindblad operator describing the decay and dephasing of the atoms. The above Hamiltonian and master equation are obtained in the absence of thermal motion of the atoms. Note that the thermal motion is completely random and isotropic, but by decomposing the velocity of atoms into three orthogonal components in the Cartesian coordinate system, we can only consider the longitudinal Doppler effect along the light propagating

*Electronic address: ycliu@tsinghua.edu.cn

direction and neglect the small transverse Doppler effect. In the presence of thermal motion, a laser beam with wave number k moving towards (away from) an atom with velocity v "sees" the atomic frequency upshifted (downshifted) by an amount kv. Thus, for an atom moving with velocity v along the direction of control laser beams, we need to replace the detunings Δ_c and Δ_s with $\Delta_c + k_c v$ and $\Delta_s + k_s v$, as the two control laser beams propagate along the same direction. For the probe field, it will "see" the same Doppler shift in the co-propagating case ($\Delta_p + k_p v$) and opposite in the counter-propagating case ($\Delta_p - k_p v$). Since the frequency differences among the three lasers are quite small compared with their absolute frequencies, we have $k_c \approx k_s \approx k_p = k$. The equations for the atomic density matrix elements take the form

$$\begin{aligned}
\dot{\rho}_{11} =&\Gamma_{31}\rho_{33} + \Gamma_{21}\rho_{22} + \Gamma_{41}\rho_{44} - \Gamma_{13}\rho_{11} + \frac{i}{2}\left(\rho_{21}\Omega_s^* - \rho_{12}\Omega_s\right), \\
\dot{\rho}_{22} =&\Gamma_{42}\rho_{44} - \Gamma_{23}\rho_{22} - \Gamma_{21}\rho_{22} + \frac{i}{2}\left(\rho_{32}\Omega_c - \rho_{23}\Omega_c^* + \rho_{12}\Omega_s - \rho_{21}\Omega_s^*\right), \\
\dot{\rho}_{33} =&\Gamma_{43}\rho_{44} + \Gamma_{13}\rho_{11} + \Gamma_{23}\rho_{22} - \Gamma_{31}\rho_{33} + \frac{i}{2}\left(\rho_{23}\Omega_c^* - \rho_{32}\Omega_c + \rho_{43}\Omega_p^* - \rho_{34}\Omega_p\right), \\
\dot{\rho}_{44} =&-\left(\Gamma_{43} + \Gamma_{42} + \Gamma_{41}\right)\rho_{44} - \frac{i}{2}\left(\rho_{43}\Omega_p^* - \rho_{34}\Omega_p\right), \\
\dot{\rho}_{21} =&-\tilde{\gamma}_{21}\rho_{21} + \frac{i}{2}\left(\rho_{31}\Omega_c + \left(\rho_{11} - \rho_{22}\right)\Omega_s\right), \\
\dot{\rho}_{31} =&-\tilde{\gamma}_{31}\rho_{31} - \frac{i}{2}\left(\rho_{32}\Omega_s - \rho_{21}\Omega_c^* - \rho_{41}\Omega_p^*\right), \\
\dot{\rho}_{41} =&-\tilde{\gamma}_{41}\rho_{41} - \frac{i}{2}\left(\rho_{42}\Omega_s - \rho_{31}\Omega_p\right), \\
\dot{\rho}_{23} =&-\tilde{\gamma}_{23}\rho_{23} + \frac{i}{2}\left(\left(\rho_{33} - \rho_{22}\right)\Omega_c + \rho_{13}\Omega_s - \rho_{24}\Omega_p\right), \\
\dot{\rho}_{42} =&-\tilde{\gamma}_{42}\rho_{42} + \frac{i}{2}\left(\rho_{32}\Omega_p - \rho_{43}\Omega_c^* - \rho_{41}\Omega_s^*\right), \\
\dot{\rho}_{43} =&-\tilde{\gamma}_{43}\rho_{43} + \frac{i}{2}\left(\left(\rho_{33} - \rho_{44}\right)\Omega_p - \rho_{42}\Omega_c\right),
\end{aligned} \tag{3}$$

where $\rho_{ij} = \rho_{ji}^*$, $\tilde{\gamma}_{21} = \gamma_{21} - i\left(\Delta_s + kv\right)$, $\tilde{\gamma}_{31} = \gamma_{31} - i\left(\Delta_s - \Delta_c\right)$, $\tilde{\gamma}_{41} = \gamma_{41} - i\left(\Delta_s - \Delta_c + \Delta_p \pm kv\right)$, $\tilde{\gamma}_{23} = \gamma_{23} - i\left(\Delta_c + kv\right)$, $\tilde{\gamma}_{42} = \gamma_{42} - i\left(\Delta_p \pm kv - \Delta_c - kv\right)$, $\tilde{\gamma}_{43} = \gamma_{43} - i\left(\Delta_p \pm kv\right)$, $\gamma_{nm} = \frac{1}{2}\left(\Gamma_n + \Gamma_m\right) + \gamma_{nm}^{\mathrm{col}}$, Γ_{nm} is the natural decay rates between level $|n\rangle$ and level $|m\rangle$, $\gamma_{nm}^{\mathrm{col}}$ is the collision-induced dephasing rate.

If the collision-induced dephasing rate is small, due to the atomic coherence, we often observe some narrow bandwidth nonlinear phenomena such as electromagnetically induced transparency, electromagnetically induced absorption or Mollow sideband-like transparency windows. But if we enhance collisions of atoms by introducing buffer gas, the dephasing rate increases and the coherence between atoms becomes weaker, then the absorption of probe laser is mainly determined by the population of atoms in level $|3\rangle$. By solving Eq. (3) in the steady state, we can numerically obtain the density matrix element $\rho_{33}\left(\Delta_s + kv, \Delta_c + kv, \Delta_p \pm kv\right)$ for atoms with velocity v, with $\pm$ corresponding to the co-propagating and counter-propagating cases, respectively. The atomic velocity along the light propagating direction obey the Maxwellian velocity distribution

$$f(v) = \frac{1}{\sqrt{\pi}u}\exp\left(-\frac{v^2}{u^2}\right), \tag{4}$$

where $u = \sqrt{2k_BT/m}$ is the most probable speed of atoms, k_B is the Boltzmann constant, T is the temperature of the atomic gas, and m is the mass of the atom. Therefore, the atomic velocity distribution of atoms in level $|3\rangle$ is given by

$$\tilde{\rho}_{33}\left(\Delta_s + kv, \Delta_c + kv, \Delta_p \pm kv\right) = \frac{1}{\sqrt{\pi}u}\exp\left(-\frac{v^2}{u^2}\right)\rho_{33}\left(\Delta_s + kv, \Delta_c + kv, \Delta_p \pm kv\right). \tag{5}$$

The above equation can also be re-written as $\tilde{\rho}_{33}^{(\mathrm{co/cou})}(v) = f(v)\rho_{33}^{(\mathrm{co/cou})}(v)$, where co/cou correspond to the co-propagating/counter-propagating cases with the sign $+/-$, respectively. Then the atom number in level $|3\rangle$ for the co-propagating/counter-propagating cases ($n_{\mathrm{co/cou}}$) can be calculated by integrating $\tilde{\rho}_{33}^{(\mathrm{co/cou})}(v)$ with respect to v.

As shown in Figs. S1(a) and S1(b), the curves of velocity distribution $\tilde{\rho}_{33}^{(\mathrm{co/cou})}(v)$ are Gaussian-like. When the collision broadening (570 MHz for 30 Torr buffer gas at 75°C) is comparable with the Doppler broadening (540 MHz), the velocity distribution in level $|3\rangle$ for co-propagating and counter-propagating cases are different [Figs. S1(a)],

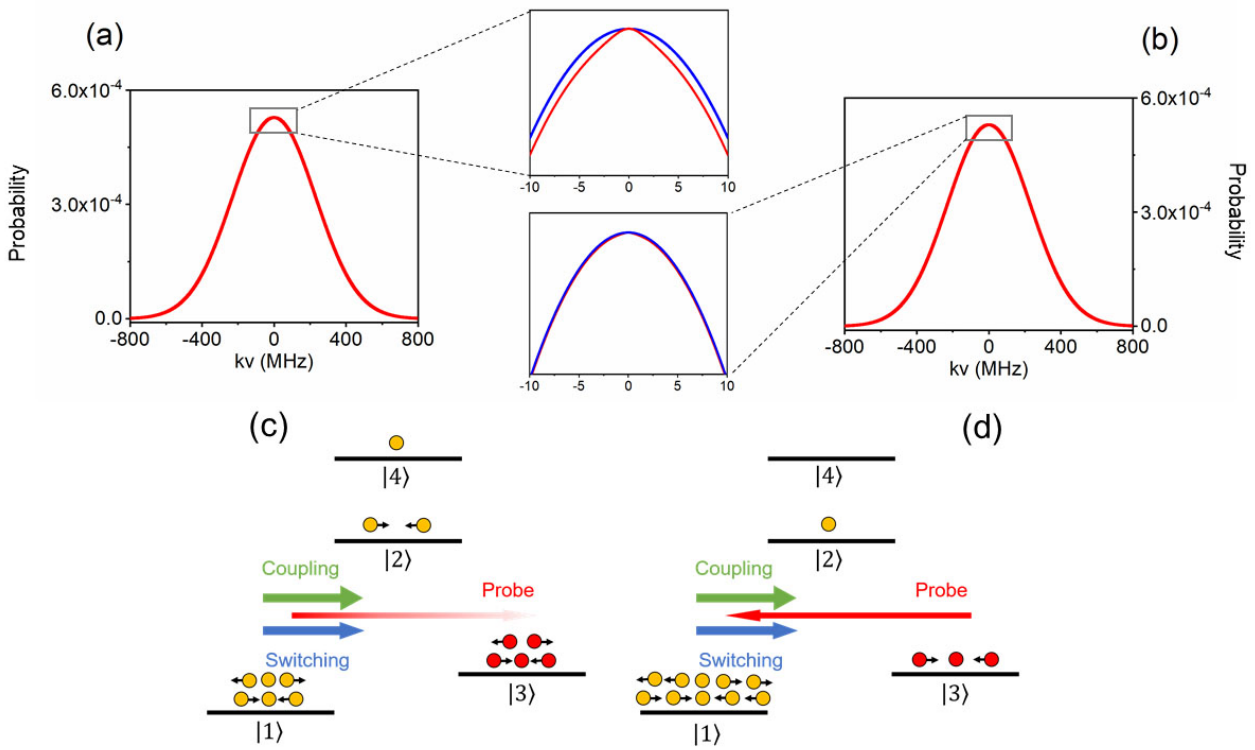

FIG. S1: (a)-(b) Atomic velocity distribution of level $|3\rangle$ for the co-propagating (blue curve) and counter-propagating (red curve) cases with collision broadening being 570 MHz (a) and 2 GHz (b). The Doppler broadening is 540 MHz. (c)-(d) Schematic diagram of atom distribution in steady state for the co-propagating (c) and counter-propagating (d) cases.

which means that the probe laser will "see" different atom numbers for co-propagating and counter-propagating cases [Figs. S1(c) and S1(d)], i.e., $n_{\rm co} \neq n_{\rm cou}$, leading to the optical nonreciprocity. As a comparison, we also plot the results for very large collision broadening (2 GHz) in and S1(b). In this case the velocity distribution for co-propagating and counter-propagating cases are almost the same, which reduces the optical nonreciprocity.

The transmission of the probe laser can be calculate using the law of absorption

$$I\left(l\right) = I\left(0\right)\exp\left(-n\sigma l\right), \tag{6}$$

where $I\left(0\right)$ is the laser intensity entering the front of the cell, $I\left(l\right)$ is the laser intensity after passing through the atoms, σ is the photon absorption cross-section whose lineshape is the Voigt profile, l is the length of the rubidium cell, n is the atomic density in level $|3\rangle$. Here n can be represented by $n_{\rm co}$, $n_{\rm cou}$ and n_0, for the co-propagating, counter-propagating and no control lasers cases, respectively. Then the corresponding transmission spectra are given by

$$\begin{aligned} T_{\rm co} &= \exp\left(-n_{\rm co}\sigma l\right), \\ T_{\rm cou} &= \exp\left(-n_{\rm cou}\sigma l\right), \\ T_0 &= \exp\left(-n_0\sigma l\right), \end{aligned} \tag{7}$$

with the results plotted in Fig. 2(b) of the main text.

II. EXPERIMENTAL SETUP

The detailed experimental setup is shown in Fig. S2. A cubic vapor cell of side length 1 cm is filled with gaseous rubidium-87 (^{87}Rb) atoms and buffer gas (helium-4 and nitrogen). For 30 Torr helium-4, 5 Torr nitrogen and temperature being 75°C, the collision-induced shift and broadening of the optical resonance line is about 120 MHz (4.6 MHz/Torr) and 570 MHz (17 MHz/Torr for helium-4, 8.86 MHz/Torr for nitrogen). The control and probe lasers are polarized by the Glan-Taylor prism (GTP) as linearly polarized light. The two control lasers have the

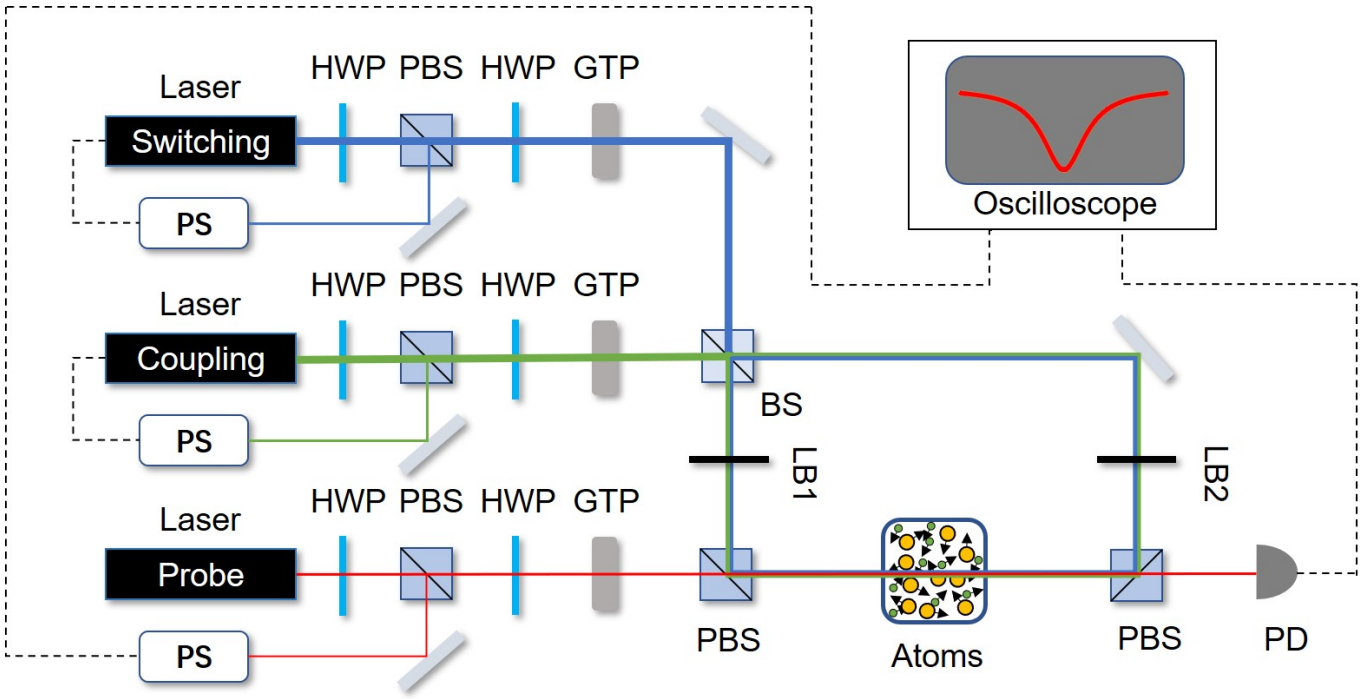

FIG. S2: Detailed experimental setup. HWP is half-wave plates; PBS is polarizing cubic beam splitters; PD is photodiode detector; BS is beam splitters; GTP is Glan-Taylor prism; LB1-2 are laser blockings; PS represents polarization spectroscopy. Solid lines in color represent optical paths, and black dashed lines represent electrical connections.

same polarization, which enter and leave ^{87}Rb cell through two polarizing beam splitters (PBS). The probe laser with polarization perpendicular to the control lasers passes directly through the cell. The radii of the coupling, switching, and probe laser beams are about 0.8, 0.8, and 0.3 mm, respectively.

In our experiment, the switching between co-propagating and counter-propagating cases are realized by changing the direction of the two control lasers. As shown in Fig. S2, we use laser blocking (LB) to block the control lasers from the opposite direction, i.e., LB1 for the counter-propagating case and LB2 for the co-propagating case. The control lasers are locked to the corresponding atomic transitions by polarization spectroscopy (PS) and part of the probe laser is split to a PS setup to monitor the frequency of the probe field. The power of the control and probe lasers are tuned by adjusting the angle of the half-wave plate (HWP). The transmission spectrum is measured by sweeping the frequency of the probe field and recording the laser intensity with photodiode detector (PD).

There is no magnetic shielding in our experiment because the splitting of energy level caused by geomagnetic field is much smaller than the collision broadening and Doppler broadening. Thus the effect of geomagnetic field can be ignored.

III. ADDITIONAL EXPERIMENT RESULTS

In this section, we present more experimental results by varying the system parameters, including the temperature, the buffer gas density, the probe laser power, the detuning and power of the control lasers.

A. Experimental results for different temperature

In our experiments we have performed a whole set of experiments at different temperatures ranging from 60°C to 100°C, with typical results plotted in Fig. S3. As we increase the temperature, both the collision broadening and Doppler broadening increases, which further reduce the transmission for the co-propagating case and increase the isolation bandwidth. At the same time, the transmission for the counter-propagating case also becomes lower, which slightly reduce the maximum isolation ratio.

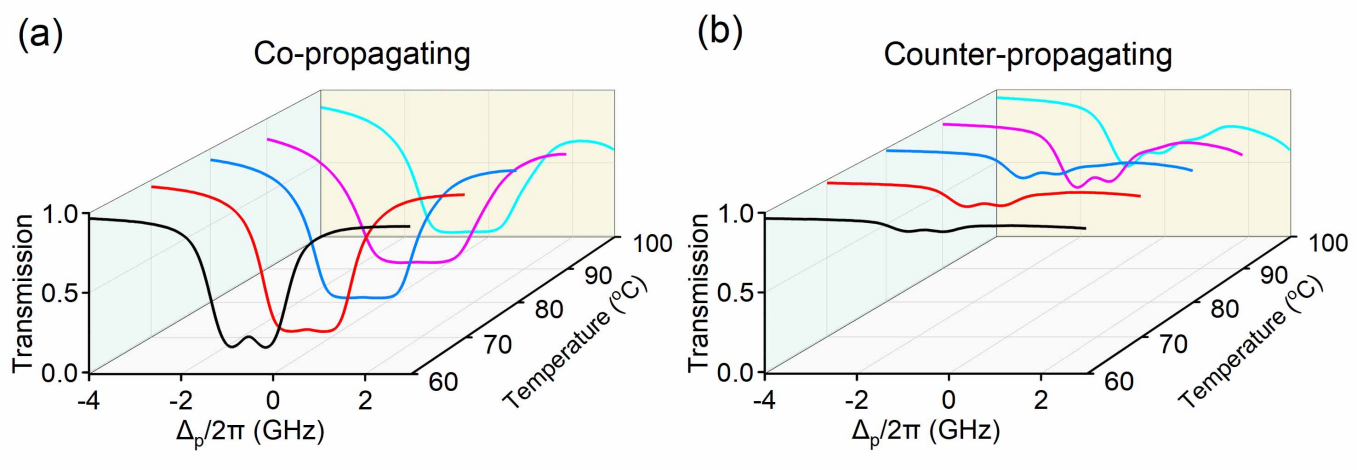

FIG. S3: (a)-(b) Normalized transmission spectra of the probe laser at different temperatures ranging from 60°C to 100°C for co-propagating (a) and counter-propagating (b) cases.

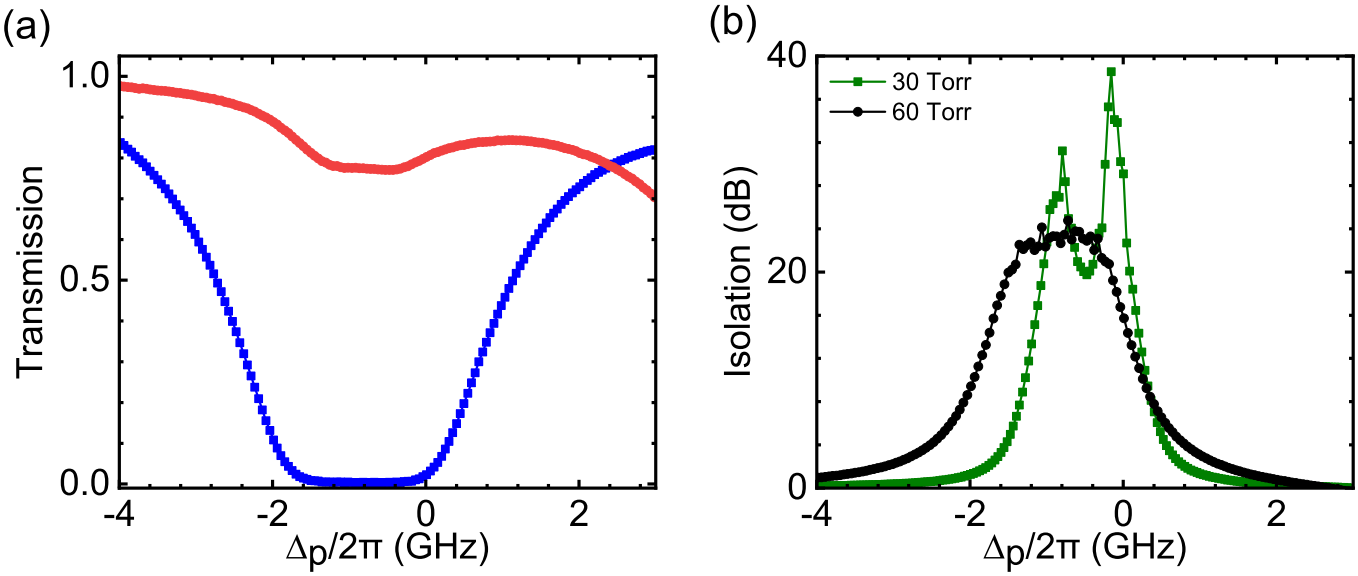

FIG. S4: (a) Typical experimental results of probe laser transmission spectra for co-propagating (red dots) and counter-propagating (blue dots) cases. (b) The isolation ratio for 60 Torr (black dots) and 30 Torr (green dots) buffer gas. The latter corresponds to the results in Fig. 1(c) of the main text.

B. Experimental results for different buffer gas density

We also performed the experiments for different buffer gas density, with the typical results for 60 Torr helium-4 plotted in Fig. S4. As a result of the stronger atomic collision, the nonreciprocal window becomes broader, together with a larger resonance frequency shift, compared with the results in Fig. 2 of the main text.

Figure S5 shows the measured probe laser transmission spectra for co-propagating and counter-propagating cases at different control laser powers. Similar to Fig. 3 in the main text, the coupling laser mainly increases the transmission of the probe laser in the counter-propagating case, while the switching laser decreases the transmission of the probe laser in the co-propagating case. The curves show broader nonreciprocal window than that in Fig. 3 of the main text due to stronger atomic collision.

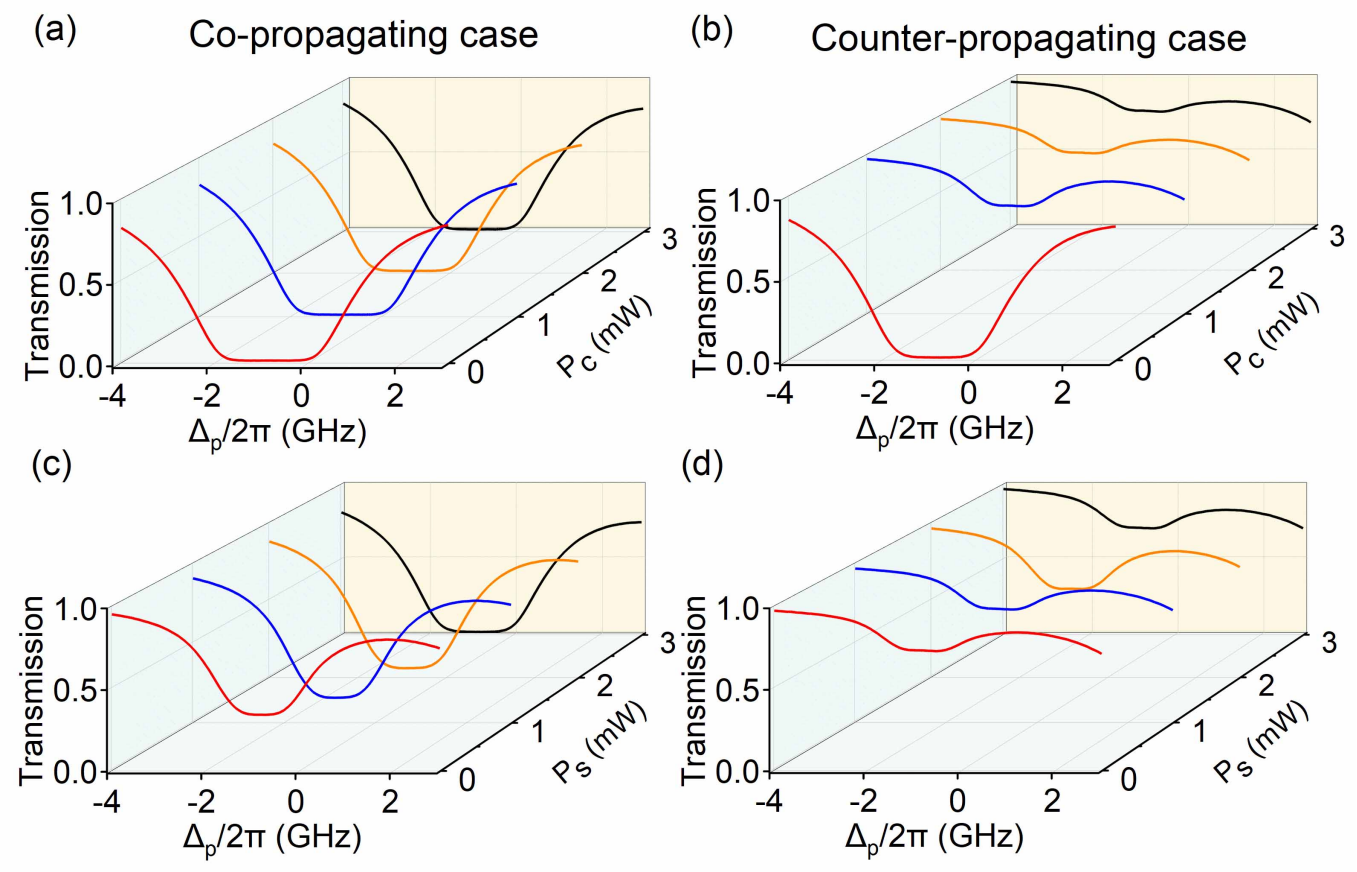

FIG. S5: (a) Transmission spectra of the probe laser for different coupling laser power P_c from 0 to 3 mW. The switching laser power is fixed at $P_s = 3$ mW. (b) Transmission spectra of the probe laser for different switching laser power P_s from 0 to 3 mW. The coupling laser power is fixed at $P_c = 3$ mW.

C. Experimental results for different probe laser power

In Fig. S6 we plot the detailed transmission spectra for different probe laser power. For probe laser power ranging from 10 μW to 150 μW, the transmission approaches 0 (for probe laser detuning from -1 GHz to 0) in the co-propagating case [Fig. S6(a)], and is relatively high in the the counter-propagating case [Fig. S6. For these probe laser power, the bandwidth for isolation ratio greater than 20 dB are above 1.2 GHz (as shown in Fig. 2(d) of the main text).

D. Experimental results for different detuning and power of the control lasers

We further studied the effect of detuning and power of the control lasers on the transmission of the probe field. Normalized transmission of the probe field versus the coupling field detuning Δ_c (switching filed detuing Δ_s) at zero switching (coupling) and probe field detunings are shown in Figs. S7(a) and S7(b) [Figs. S7(c) and S7(d)]. Without the coupling field, the nonreciprocal transmission disappears (red curves). Without the switching field, the nonreciprocity still exists, but the isolation ratio is quite small since the co-propagating transmission is not low enough (blue curves). In this case the atoms can be viewed as V-type level system involving only three energy levels. The effect of the switching field is lowering the transmission of probe field in the co-propagating case (from blue to black curves), while the effect of the coupling field is increasing the transmission of probe field in the counter-propagating case (from red to black curves). The combination of switching and coupling lasers leads to very high isolation ratio.

In Figs. S7(c) and S7(d), their is another nonreciprocal window near $\Delta_s/2\pi \approx -6.8$ GHz. This is because in this case the switching field here will driving the atomic transition $|2\rangle \Leftrightarrow |3\rangle$, meaning that the switching field actually plays the role of the coupling field. This is also consistent with the results in Fig. 4 of the main text.

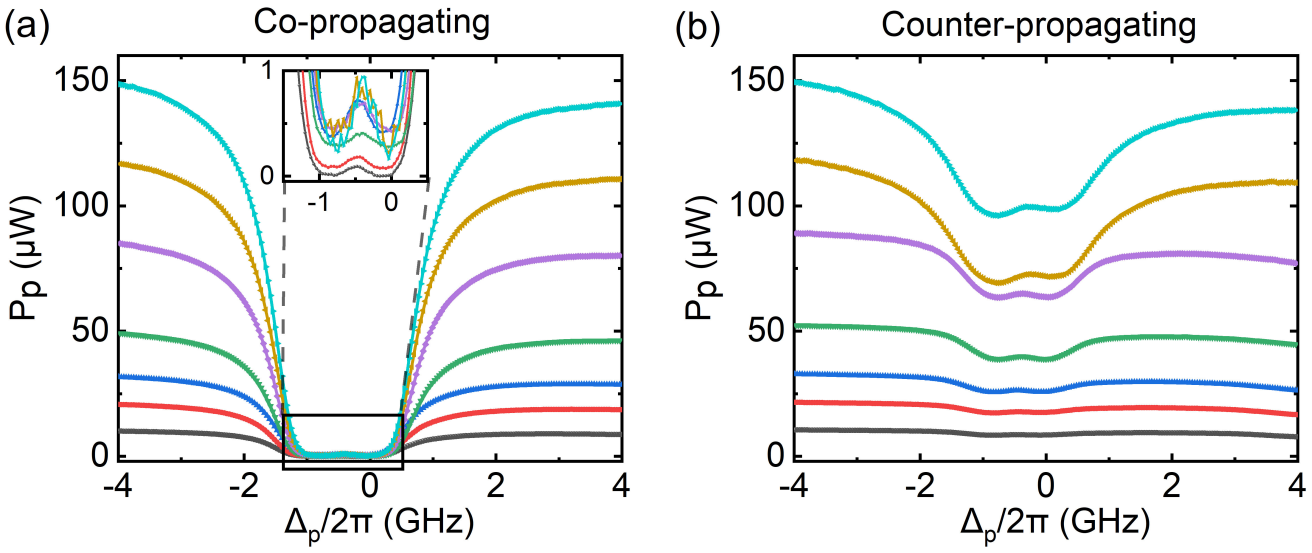

FIG. S6: Transmission spectra (unnormalized) of the probe laser with different probe laser power ranging from 10 μW to 150 μW for co-propagating (a) and counter-propagating (b) cases. In the (a), the zoom-in view insert shows the transmission of the probe laser when the detuning is near zero.

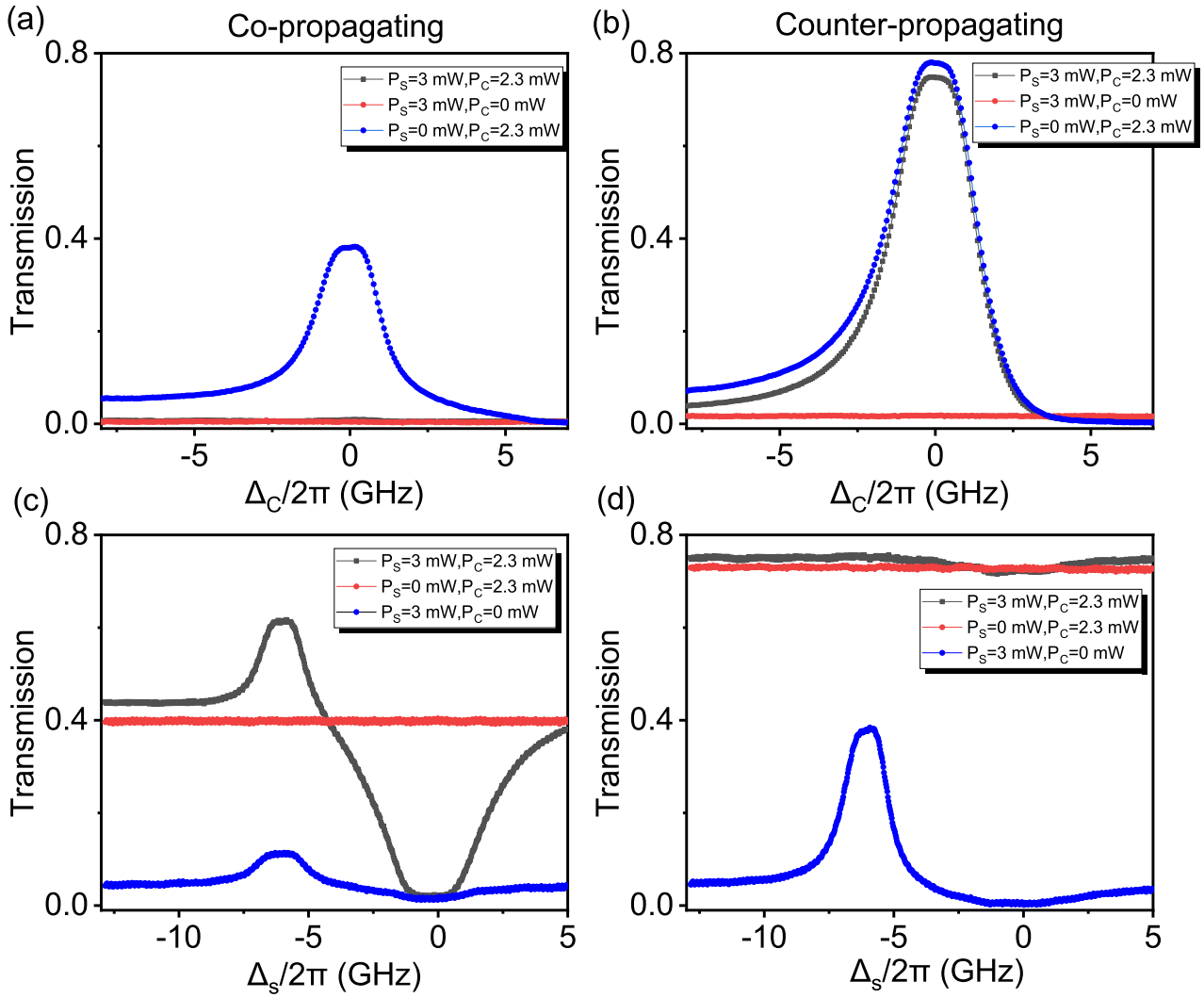

FIG. S7: (a)-(b) Normalized transmission spectra of the probe laser versus the coupling field detuning Δ_c at different switching and coupling field power, for co-propagating (a) and counter-propagating (b) cases. (c)-(d) Same as (a) and (b) except that the horizontal axis is replaced by the switching field detuning Δ_s.